

Evaluation of the effect of microphone cavity geometries on acoustic imaging in wind tunnels

van Dercreek, Colin; Merino-Martínez, Roberto; Sijtsma, Pieter; Snellen, Mirjam

DOI

[10.1016/j.apacoust.2021.108154](https://doi.org/10.1016/j.apacoust.2021.108154)

Publication date

2021

Document Version

Final published version

Published in

Applied Acoustics

Citation (APA)

van Dercreek, C., Merino-Martínez, R., Sijtsma, P., & Snellen, M. (2021). Evaluation of the effect of microphone cavity geometries on acoustic imaging in wind tunnels. *Applied Acoustics*, 181, Article 108154. <https://doi.org/10.1016/j.apacoust.2021.108154>

Important note

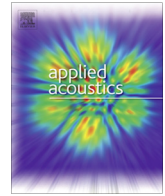
To cite this publication, please use the final published version (if applicable).
Please check the document version above.

Copyright

Other than for strictly personal use, it is not permitted to download, forward or distribute the text or part of it, without the consent of the author(s) and/or copyright holder(s), unless the work is under an open content license such as Creative Commons.

Takedown policy

Please contact us and provide details if you believe this document breaches copyrights.
We will remove access to the work immediately and investigate your claim.



Evaluation of the effect of microphone cavity geometries on acoustic imaging in wind tunnels[☆]

Colin VanDercreek^{a,*}, Roberto Merino-Martínez^a, Pieter Sijtsma^b, Mirjam Snellen^a

^a Faculty of Aerospace Engineering, Delft University of Technology, Kluyverweg 1, 2629 HS Delft, The Netherlands

^b PSA3, 9493TE De Punt, The Netherlands

ARTICLE INFO

Article history:

Received 30 November 2020

Received in revised form 26 April 2021

Accepted 26 April 2021

2010 MSC:

00–01

99–00

Keywords:

Microphone arrays

Aeroacoustics

Wind-tunnel measurements

Boundary layer noise

Cavity

Beamforming

ABSTRACT

Aeroacoustic measurements performed by flush-mounted microphone arrays on the walls of closed-section wind tunnels are contaminated by the hydrodynamic pressure fluctuations of the wall's boundary layer. This study evaluates three different microphone cavity geometries for mitigating this issue. Their improvement to the signal-to-noise ratio (SNR) and the accuracy of their acoustic imaging results are compared to a flush-mounted microphone array. The four geometries include: (1) an array of flush-mounted microphones as the baseline, (2) a cylindrical hard-plastic cavity with a countersink, (3) a conical cavity made of melamine acoustic absorbing foam, and (4) a conical cavity with star-shaped protrusions, also made of melamine. The three arrays with cavities were covered with a steel-wire cloth to reduce the boundary layer fluctuations at the microphone while the baseline array was uncovered. Two sound sources were tested in an aeroacoustic wind tunnel for assessing the performance of the different cavities: a speaker placed outside the flow and a distributed sound source generated by a flat plate inside of the flow. When using conventional frequency domain beamforming, both cavities made of melamine offer up to a 30 dB increase in SNR with respect to the flush-mounted case, followed by the hard-walled cavity with up to a 20 dB increase. This is a 20 dB improvement when compared to the single microphone cases. The melamine cavities also provide cleaner acoustic source maps and accurate spectral estimations for a wider frequency range. The effect of cavity placement and geometry on the coherence, which affects the beamforming analysis of the acoustic signal was negligible for all cases. Distributed sound source measurements using the three arrays agreed with predictions using the Brooks, Pope, and Marcolini (BPM) model, showing that the cavities could detect vortex shedding that was undetectable by the flush array.

© 2021 The Author(s). Published by Elsevier Ltd. This is an open access article under the CC BY license (<http://creativecommons.org/licenses/by/4.0/>).

1. Introduction

Aeroacoustic experiments in wind tunnels are often performed in open-jet facilities as they allow for placing the microphones outside of the flow [1]. However, the aerodynamic conditions in open-jet wind tunnels [2] are less well-controlled than in closed-section wind tunnels and require corrections to account for the acoustic signal refracting as it passes through the shear layer. Acoustic measurements in closed-section wind tunnels, on the other hand, are affected by several sources of noise inherent to wind tunnels [3], including the ones from the turbulent boundary layer (TBL) along

the tunnel's walls, the tunnel's machinery, and reflections that propagate within the tunnel's closed test section. For this application, microphones are typically mounted flush and, consequently, the measurements are contaminated with TBL noise. The present article focuses on the effect cavities, which minimize the influence of the TBL hydrodynamic noise (pressure fluctuations), have on single microphone acoustic measurements and acoustic imaging measurements using a microphone array.

The signal-to-noise ratio (SNR) of the microphone array when measuring the far-field emissions of an acoustic source can be increased by attenuating the level of TBL noise at the microphone. This can be achieved in two ways. First, employing acoustic beamforming and applying techniques that average out the incoherent noise, which includes TBL noise [4]. These techniques include removing the main diagonal of the cross-spectral matrix (CSM) or advanced imaging methods, such as CLEAN-SC [5] and others

[☆] This work is part of the research program THAMES with project number 15215, which is (partly) financed by the Dutch Research Council (NWO).

* Corresponding author.

E-mail address: c.p.vandercreek-1@tudelft.nl (C. VanDercreek).

Nomenclature

Nomenclature

a	Cavity radius
c	Speed of sound
C_{xy}	Coherence between signals x and y
f	Sound frequency
H	Boundary layer shape factor
He	Helmholtz number
L_p	Sound pressure level
P_{xx}	Auto spectral density of signal x
P_{xy}	Cross-spectral density of signals x and y
St	Strouhal number
U_∞	Free stream velocity
x, y, z	Cartesian coordinates
Δf	Frequency resolution
ΔL_p	Difference in sound pressure level
δ_{99}	Boundary layer thickness

δ^*	Boundary layer displacement thickness
Θ	Boundary layer momentum thickness
ω	Angular frequency

Abbreviations

BPM	Brooks, Pope, and Marcolini
CFDBF	Conventional Frequency Domain Beamforming
CSM	Cross-spectral matrix
HWA	Hot-wire anemometry
NI	National Instruments
ROI	Region of integration
SNR	Signal-to-noise ratio
SPI	Sound Power Integration
TBL	Turbulent boundary layer

[6,7]. Secondly, recessing the microphones behind an acoustically transparent covering [8] and within cavities [9,10] further reduces the measured TBL noise. The latter approach normally uses a fine stainless steel cloth or a Kevlar sheet [8,11,12], which reduces the intensity of the boundary layer's hydrodynamic pressure fluctuations that enter the cavity but allows for the propagation of acoustic waves. The geometry of the cavity itself also has a significant effect on the amount of attenuation. Previous literature focused on studying the influence that different cavity geometric parameters, such as depth [13] and countersink [9], had on the reduction of TBL noise for a single microphone. However, there is a lack of research in quantifying the effects that different cavities have on microphone array measurements, in terms of TBL noise attenuation and accuracy of the acoustic imaging results. This article aims to quantify the impact different cavities have on aeroacoustic measurements by comparing three microphone arrays equipped with different cavity geometries with respect to a flush-mounted baseline array, all of which using the same microphone distribution. Both SNR (microphone level) and acoustic imaging performance are assessed.

The cavity shape and wall material have a significant influence on its performance with respect to TBL noise attenuation [9,10]. The relevant geometric parameters include: cavity depth, cavity aperture area, aperture area reduction with respect to depth, wall material (acoustic absorbing or not), and the presence of an acoustically transparent material (in this case a stainless steel wire cloth) over the top of the cavity. In general, increasing the depth, and reducing the aperture area with cavity depth (i.e. conical shape) all attenuate the measured TBL noise [9,10].

In general, for flow over a cavity, the wave numbers associated with TBL noise are much higher than the typical acoustic wave numbers of interest. This is due to the speed of sound being considerably greater than the TBL convective velocity. Therefore, considering the excitation of acoustic modes by the TBL, the dispersion relation for acoustic waves only permits imaginary wave numbers in the direction perpendicular to the wall (i.e. into the cavity), which means an exponential decay. For cavities with circular apertures, the TBL excitation is decomposed in duct modes. If the hydrodynamic wavelength is short compared to the aperture area, modes with imaginary axial wave numbers (cut-off modes) prevail. Specifically, the acoustic wave number is imaginary (cut-off) when a mode's radial wavenumber is larger than the Helmholtz number, $He = \frac{\omega a}{c}$, where ω is the angular frequency, c is the speed of sound, and a is

the cavity radius [14]. For Helmholtz numbers less than 1.84, all modes are cut-off, except for the plane duct mode. If the wavelength is long with respect to the aperture radius (low frequency, small aperture, high convection speed) then mainly the plane duct mode is excited. In that case, there is not much TBL noise attenuation. For the cavities considered in this article, the radii are on the order of 10 mm, and the frequency range of interest is in between 250 Hz and 10 kHz, therefore, only the plane wave is cut-on. Other acoustic modes decay exponentially with increasing cavity depth. When the radius of the cavity is no longer constant with depth, such as for a countersink, further attenuation occurs. This is due to the fact that the change in area results in a transmission loss for the propagating wave [10] due to the change in acoustic impedance.

Cavity walls made of sound absorbing materials, such as melamine, reduce the intensity of reflections and standing wave amplitudes within the cavity. This results in a further reduction in the TBL noise at the microphone compared to hard walled cavities. Finally, covering the cavity with an acoustically transparent material, such as a fine stainless steel wire cloth or a Kevlar sheet [8,11], reduces the transmission of the TBL's hydrodynamic fluctuations into the cavity. The latter results in as much as a 10 dB additional reduction in TBL noise at the microphones. The cavities in this study have both hard and soft walls, a stainless steel cloth covering, and different depths and aperture areas.

In addition to the spectra measured by the individual microphones, conventional frequency domain beamforming (CFDBF) [15] is employed to locate and quantify the sound pressure level (L_p) of the sound sources. Since TBL noise is generally incoherent from microphone to microphone [16], beamforming itself also improves the SNR of the measurements by reducing the effects of this noise source. It should be noted that, whereas the use of some advanced acoustic imaging algorithms [5–7,17] can further reduce the effect of TBL and background noise, most of them rely on the results of CFDBF. Thus, this article only considers CFDBF results, since improving these is consequently expected to also improve the results of advanced methods. Additionally, the effect of applying coherence weighting [18] to the microphone signals was briefly investigated.

The measurements were performed in the anechoic open-jet wind tunnel of Delft University of Technology (A-Tunnel) [19] where a microphone array was used to measure a speaker emitting white noise located outside of the airflow and the trailing edge noise of a flat plate.

The objective of this article is to quantify the SNR improvement due to different cavity geometries for different flow speeds. The acoustic measurements are evaluated in terms of the integrated L_p and SNR when applying CFDBF with diagonal removal. Additionally, the coherence levels between cavities are evaluated for the speaker measurements to quantify the effect different cavity designs, especially due to the presence of a stainless steel cloth, have on the coherence of the acoustic signal.

This article is organized in the following manner: *Experimental set-up* which discusses the test facility, array design, and measurements; *Experimental results* which discusses the boundary layer measurements, the acoustic measurements of the speaker, the influence of the TBL on the acoustic measurements for single microphones and the array, the results of the distributed sound source measurements, and the resulting effect of cavity geometry on signal coherence; and finally the *Conclusions*.

2. Experimental set-up

2.1. Wind tunnel facility

The test section of the A-Tunnel is located within an anechoic chamber that measures 6.4 m (length) \times 6.4 m (width) \times 3.2 m (height). The chamber is covered with acoustic absorbing foam wedges, which provides free-field sound propagation properties for frequencies higher than 200 Hz [20,19], thus reducing unwanted reflections from walls, floor, and ceiling. An open-jet geometry configuration was employed for this study, with one of the (rectangular) nozzle edges extended with a plate in which the microphones were mounted. With this geometry the sound perceived by the microphones is dominated by the TBL noise over the array, as would be the case in a closed-section wind tunnel. This set-up also allows for a speaker to be placed outside of the flow, avoiding the interaction of the flow with the speaker and its support hardware. The rectangular nozzle employed has an exit

area of 0.7 m \times 0.4 m, see Fig. 1a, and provides a maximum flow velocity, U_∞ , of 34 ms⁻¹. For this experiment flow velocities of 20 and 34 ms⁻¹ are considered.

2.2. Microphone array

The acoustic array consists of 16 microphones with two additional flush-mounted reference microphones. These 16 microphones are placed in a sunflower pattern [21] with an array diameter of approximately 350 mm as seen in Fig. 1b. The layout was optimized [22] to minimize sidelobes and, thus, maximize the dynamic range between the frequencies of 2 kHz and 4 kHz. This design was predicted to have a maximum dynamic range of 9.6 dB based on a simulated monopole source [22]. Having only 16 microphones with this array diameter, limits the dynamic range and beamwidth compared to typical acoustic arrays that feature more microphones spread out over a larger area. The usable frequency range of this array is 1075 Hz to 9187 Hz. Usability for the lower frequency limit is defined as the main lobe width (3 dB below its peak value) for a point sound source placed in the direction normal to the array's center fitting within a 45° wide beam with respect to the same direction. The usability of the upper frequency limit is defined as the sidelobes being 8 dB below the peak L_p of the main lobe. This array configuration was chosen to limit the complexity and allow for the experiment to be carried out for different cavity geometries.

G.R.A.S. 40PH analog free-field microphones [23] were used in the array which feature an integrated constant current power amplifier and a 135 dB dynamic range. Each microphone has a diameter of 7 mm and a length of 59.1 mm. All the microphones were calibrated individually using a G.R.A.S. 42AA pistonphone [24] following the guidelines of Mueller [3]. The transducers have a flat frequency response within ± 1 dB from 50 Hz to 5 kHz and within ± 2 dB from 5 kHz to 20 kHz. The data acquisition system consisted of 4 National Instruments (NI) PXIe-4499 sound and

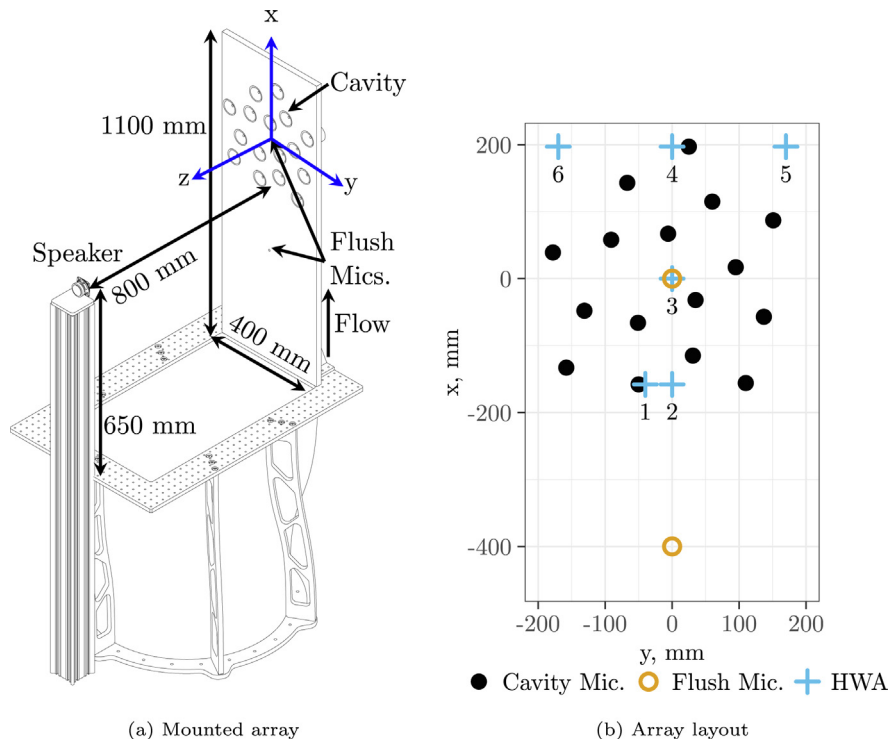


Fig. 1. Experimental set-up at the A-Tunnel. (a) Array mounted on nozzle. (b) Array microphone distribution with hot-wire anemometry (HWA) measurement locations as seen from in front.

vibration modules with 24 bits resolution. The boards are controlled by a NI RMC-8354 computer via a NI PXIe-8370 board.

The array cavities were installed in a 1.1 m × 0.4 m poly-carbonate plate, see Fig. 1a. Two different plates were manufactured: one with 7 mm diameter holes for the flush-mounted microphones (array 1) and a second one (arrays 2–4) that is covered with a 500 thread per square inch (#500) stainless steel cloth with a thread diameter of 0.025 mm. Arrays 2–4 are the arrays for each cavity type, as defined in the *Cavity design* section. The second plate features 16 threaded holes of 50 mm diameter at the microphone positions, which allowed for different cavity inserts to be installed for each array. The center of the microphone distribution ($x = y = z = 0$ m) is located 800 mm downstream of the nozzle exit plane in order to allow for the boundary layer along the plate to become fully turbulent. The flush-mounted reference microphones were mounted along the array center line ($y = 0$ m) with one at $x = 0$ m and the other was located upstream at $x = -0.4$ m, as seen in Fig. 1b.

2.3. Cavity design

Three cavity geometries were designed to compare against the baseline flush-mounted microphone array, array 1. These cavities are subsequently referred to as arrays 2, 3, and 4. The cavities in array 2 are made of a poly-carbonate material and, therefore, feature hard walls. It features a 45° countersink at the top and has a diameter of 10 mm and a depth of 10 mm. The schematic of this cavity can be seen in Fig. 2. This geometry was chosen based on it being the most effective shape for attenuating TBL noise in a previous experiment [10]. The cavity for array 3 features soft walls made of melamine foam. It has a conical shape and features 10 evenly distributed ridges. The ridges were included to study whether this cavity's performance would be different than a perfectly conical cavity. These ridges were thought to better attenuate azimuthal modes [25]. Array 4 features cavities made of melamine foam with the same conical geometry as cavity 3 but without the ridges. The cavities of arrays 3 and 4 were installed in a threaded poly-carbonate insert with the same outer mold line as those from array 2. The cavities for arrays 3 and 4 are derived from a confidential design. The cavities of arrays 2, 3, and 4 were covered with the aforementioned stainless steel cloth.

2.4. Hot-wire anemometry (HWA)

Hot-Wire Anemometry (HWA) data were measured at 6 locations and for flow speeds of 20 and 34 ms⁻¹. This was done to verify that the untripped boundary layer was turbulent and attached,

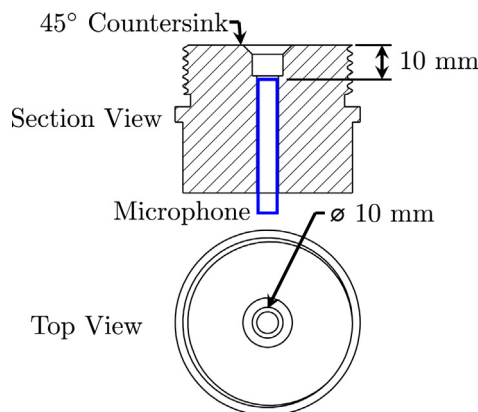


Fig. 2. Example shape and dimensions of the hard walled cavity used in array 2 for this experiment. All three cavity types were mounted in similar holders, indicated by the cross-hatched area.

especially near the upper edges of the plate. These 6 locations include three points along the top of the plate, two points along the center line, and one point just over a cavity, see Fig. 1b. The coordinates of these points are contained in Table 1 using the coordinate system defined in Fig. 1a. A calibrated Dantec 1-channel hot-wire probe was used. The sampling frequency was 50 kHz and each point was measured for 10s. These measurements were performed for both the baseline flush-mounted array which was made of smooth poly-carbonate and for the other arrays which were covered by a stainless steel cloth to determine whether this cloth affected the boundary layer.

2.5. Acoustic measurements

A single Visaton K 50 SQ speaker [26] was mounted at a distance 800 mm normal to the array. This position is outside of the flow to avoid additional noise sources due to shear layer impingement. It was located 650 mm downstream from the nozzle outlet (at $x = -150$ mm), and aligned with the axis of the jet, as seen in Fig. 1a. The speaker has a baffle diameter of 45 mm and an effective piston area of 12.5 cm². The frequency response ranges between 250 Hz and 10 kHz and a maximum power of 3 W. The speaker was used to emit white noise with an overall sound pressure level ($L_{p,overall}$), measured at the array center (without flow), of 64 dB.

The sampling frequency of the acoustic recordings was 51.2 kHz. The signal was sampled for a duration of 45 s. CFDBF was applied to the acoustic data with diagonal removal. The CSM is calculated using 4096 samples with a 50% overlap using Hanning windowing. The scan grid is located 0.8 m away from the array in the z direction, at the speaker plane, and centered at the origin of the coordinate reference system shown in Fig. 1a. The scan grid is 1 m × 1 m with a spacing between scan points of $\Delta x = \Delta y = 0.01$ m. The frequency spectra were obtained per microphone and by integrating the source maps using the Sound Power Integration (SPI) technique within a region of integration (ROI) [16,27,28,7] covering the speaker's position. The acoustic spectra, shown in subsequent sections, are presented for the frequencies between 250 Hz and 10 kHz because the beamforming array was optimized for a maximum frequency of 10 kHz and due to the maximum frequency response of the speaker.

2.6. Distributed acoustic source

A distributed line source was generated at the trailing edge of a flat plate mounted at $z = 0.35$ m from the microphone array plane. The flat plate was mounted along the jet axis and held by two support plates, as shown in Fig. 3. The plate was 0.4 m wide and 1.0 m long and was mounted with a 0° angle of attack. The trailing edge had a thickness of 1 mm and was located at $x = 0.16$ m downstream of the array center point. The flat plate was tripped at 5% of the chord from the leading edge and the estimated boundary layer displacement thickness at the trailing edge, δ^* is 0.0028 m, from the expression, $\delta^* = \frac{0.048x}{Re^{1/5}}$, where x is the streamwise position and Re is the chord-based Reynolds number [29]. This plate was chosen to provide a more representative test case [30] for aeroacoustic applications. However, the details with respect to the noise generating mechanisms by this trailing edge are beyond the scope of this article.

3. Experimental results

3.1. Boundary layer measurements

The boundary layer properties calculated from the HWA measurements show that the boundary layer characteristics are

Table 1

Hot-Wire Anemometry measurement locations with boundary layer statistics for the $U_\infty = 20 \text{ ms}^{-1}$ and 34 ms^{-1} cases for the stainless steel cloth covered array used for arrays 2, 3, and 4.

	Point 1		Point 2		Point 3		Point 4		Point 5		Point 6	
x, mm	-158		-158		0		197		197		197	
y, mm	40		0		0		0		-170		170	
$U_\infty, \text{ ms}^{-1}$	20	34	20	34	20	34	20	34	20	34	20	34
$\delta_{99}, \text{ mm}$	29.4	33.4	27.7	33.5	33.0	35.4	31.8	32.4	44.5	41.3	39.2	34.9
$\delta^*, \text{ mm}$	4.21	4.25	3.74	4.34	4.94	5.19	4.49	4.60	3.59	4.08	4.42	3.78
$\Theta, \text{ mm}$	3.23	3.28	2.95	3.41	3.75	3.97	3.45	3.56	2.96	3.34	3.58	3.11
H	1.30	1.29	1.27	1.27	1.32	1.31	1.30	1.29	1.21	1.22	1.23	1.22

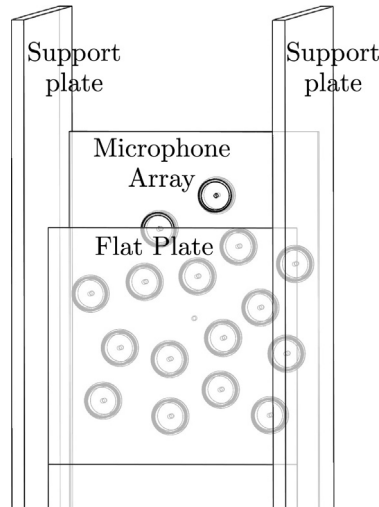


Fig. 3. Flat plate mounted used for distributed acoustic source with array 4 pictured.

consistent at the several spanwise and streamwise positions on the array. Table 1 lists the measurement locations as well as the boundary layer thicknesses δ_{99} , displacement thicknesses δ^* , momentum thicknesses Θ , and the shape factors H . The data shown were measured for a free stream flow velocity of $U_\infty = 20 \text{ ms}^{-1}$ for the array covered with the stainless steel cloth. Measurements were also taken for the $U_\infty = 34 \text{ ms}^{-1}$ case in order to verify consistency in the boundary layer characteristics at different velocities. Additionally, measurements were taken for array 1 which has a smooth surface to quantify the difference due to the surface roughness. For the 20 ms^{-1} case with stainless steel cloth covering, the boundary layer was turbulent as defined by the shape factor, H , being between 1.2 and 1.4 for all cases indicating a turbulent flow regime. The regions near the spanwise edges of the plate (points 4 and 6) show no significant changes from the flow near the plate center line. The HWA measurements taken for 34 ms^{-1} are similarly turbulent and consistent across the array. The values for the smooth array 1 are not significantly different from those of the array covered with the stainless steel cloth. For the stainless steel cloth covered array for the 34 ms^{-1} case, the TBL has a shape factor of $H = 1.29$ and boundary layer thickness of $\delta_{99} = 32.4 \text{ mm}$ as measured at point 4. For the smooth baseline array 1, the characteristics are: $H = 1.31$ and $\delta_{99} = 36.4 \text{ mm}$. H has an estimated 95% confidence interval of ± 0.1 and δ_{99} has an estimated confidence interval of $\pm 3.9 \text{ mm}$. This consistency between the different cases, reduces the likelihood of any differences between arrays being attributable to differences in the TBL that forms over the stainless steel cloth covered arrays and the baseline case.

3.2. Turbulent boundary layer (TBL) noise attenuation

The baseline flush-mounted microphone array (array 1) presents the highest TBL noise levels. This is expected behavior as the TBL pressure fluctuations were impinging directly on the microphones. All three cavity geometries considered in this article have a significant effect on the measured TBL noise. Fig. 4a shows the one-third-octave band TBL spectra for the flush-mounted microphone and each cavity for both flow velocities considered. Fig. 4b depicts the relative reduction in TBL level with respect to the values measured by array 1 (i.e. $\Delta L_p = L_{p_{\text{cavity}}} - L_{p_{\text{array1}}}$) in one-third-octave bands for arrays 2, 3, and 4. These results represent the average spectra measured by the 16 microphones in each array (without applying beamforming) and were obtained without an acoustic source being present, i.e. simply with the wind tunnel operating at the velocities specified. For the case of 20 ms^{-1} , array 2 provides a maximum reduction in TBL noise of 25 dB between 3 kHz and 4 kHz, whereas arrays 3 and 4 show an even better performance, demonstrating a reduction of 40 dB between 2.5 kHz and 6 kHz. The TBL attenuation increases with frequency due to the increasing effectiveness of the cavity. For the higher flow velocity case of 34 ms^{-1} , all the curves shift to higher frequencies and provide slightly higher maximum reductions in TBL noise. Fig. 4c contains the same values as Fig. 4b but with the frequency axis expressed in terms of the Strouhal number, $St = f \delta^* / U_\infty$, based on the free stream velocity and a reference distance of the boundary layer displacement thickness, δ^* as measured at the array center, point 4 as seen in Fig. 1b. A very good agreement is observed for the two sets of curves at different flow velocities, as expected, except for array 2 for $St \geq 0.4$ indicating that the behavior in this region may be dominated by acoustic behavior given its similarity to the acoustic transmission function seen in Fig. 5b. This Strouhal number corresponds to a frequency of 6 kHz, which will be discussed in the next section.

In order to increase the SNR of the acoustic measurements, the cavities' effect on the acoustic measurements with respect to the free-field must be smaller than that of TBL. This relationship will be discussed in the next subsection.

3.3. Acoustic measurements with the speaker without flow

Fig. 5a shows the one-third-octave band spectra obtained by each array for the case with the speaker emitting white noise with no flow. A microphone placed in the free-field was used to characterize the signal. The free-field measurements were made by placing a free-field microphone on a tripod at the same location as where the cavity closest to the array center would be. The spectra for the array measurements shown here were obtained from beamforming. However, similar results are obtained from averaging the spectra from the array microphones, since the source is almost in the centre of the array and no flow is present. For frequencies higher than 2 kHz, array 2 presents higher L_p values than

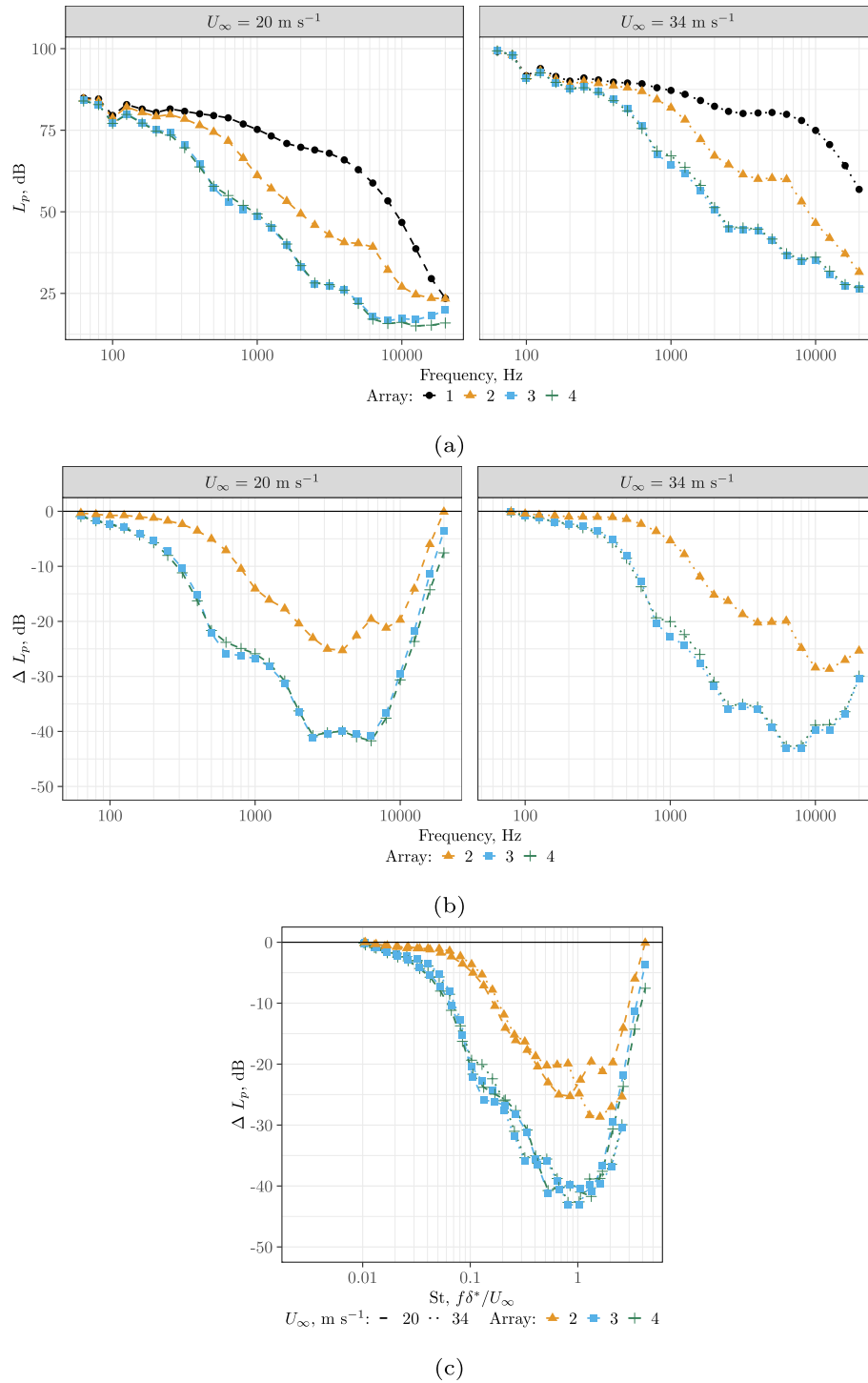


Fig. 4. Relative increase in the attenuation of TBL spectral energy of the averages over 16 microphones for arrays 1, 2, 3 and 4 for $U_\infty = 20 \text{ m s}^{-1}$ and 34 m s^{-1} . (a) Measured TBL spectra, absolute frequencies, (b) Change in spectra with respect to array 1, absolute frequencies, (c) Change in spectra with respect to array 1, non-dimensional frequencies (St).

the baseline array 1 (flush-mounted microphones), whereas arrays 3 and 4 measure consistently lower L_p values. Fig. 5b shows the relative values of $\Delta L_p = L_p - L_{p, \text{Array1}}$ of arrays 2–4 with respect to array 1 as well as the free field microphone. The results for the free-field microphone indicate the expected 6 dB increase for the baseline array due to the doubling of the pressure at the interface due to the reflection. As a general trend, the differences in L_p for the

arrays seem to increase for higher frequencies, achieving maximum ΔL_p values of 11.2 dB for array 2 at 6.3 kHz and a minimum of -9.3 dB for arrays 3 and 4 at 8 kHz. The sound amplification observed from array 2, is most likely due to standing waves amplified by the hard walls in the cavity. This acoustic excitation was also observed in a eigenfrequency analysis performed using the COMSOL finite element package (not shown here). The sound

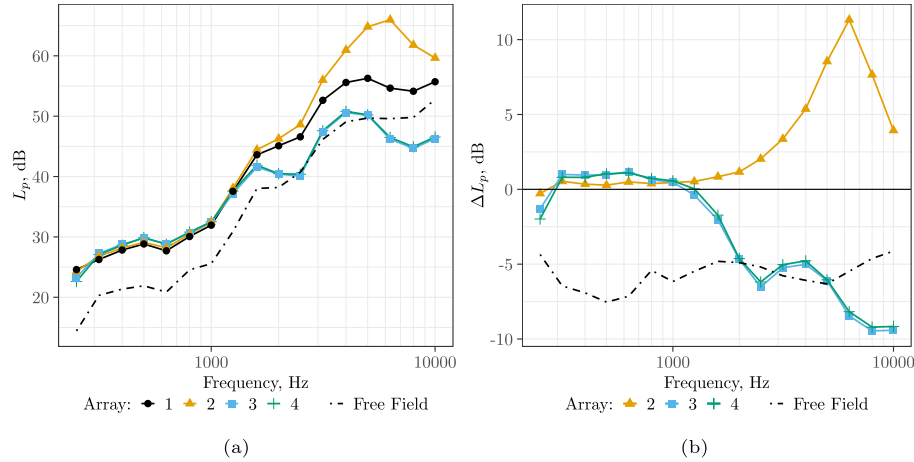


Fig. 5. (a) Comparison of the SPL one-third-octave band spectra emitted by the speaker by the four arrays with no flow ($U_\infty = 0 \text{ ms}^{-1}$) and the measurements taken by a free field microphone. (b) Relative ΔL_p values with respect to array 1 for arrays 2–4 and with respect to a single flush microphone for the free-field case.

reduction for the case of arrays 3 and 4 is due to the sound absorbing material reducing these standing waves and the cavity shape attenuating the acoustic signal.

It is evident that the cavities influence the measurement of the signal of interest. To account for this, the measured ΔL_p can be used to correct acoustic array measurements. This was performed for the speaker with flow and distributed noise sound measurements discussed later in Sections 3.4 and 3.5. Given that the previous section shows that the cavities reduce the TBL by 25 to 40 dB which is more than their effect on the acoustic signal, the SNR is increased with all cavities.

3.4. Acoustic measurements with the speaker with flow

3.4.1. Individual microphone

The combined effect of the cavities on the TBL noise and acoustic measurements is discussed in this section. Since the TBL is attenuated more than the acoustic signal by the cavities, an improvement of the SNR is expected. Fig. 6 shows the independence of the acoustic signal from the hydrodynamic TBL noise. This is evident from the close agreement of the measurements for the simultaneous presence of the TBL with the acoustic source and the summation of the independently measured TBL only and

source only cases. The summation is calculated as the sum of acoustic powers (i.e. before transforming to the decibel scale). With this assumption, we can calculate the SNR as $\text{SNR} = L_{p,\text{signal}} - L_{p,\text{TBL}}$ with $L_{p,\text{signal}}$ being the level of the acoustic signal measured without flow (Fig. 5a) and $L_{p,\text{TBL}}$ being the TBL noise measured without the speaker (Fig. 4a). The results are shown in Fig. 7. From this figure we see a significant improvement in SNR due to the cavities with a dependence on flow speed. The maximum SNR for the 20 ms^{-1} case is 25 dB and for the 34 ms^{-1} case is a much lower 8 dB, which is expected since TBL noise scales with velocity. Also shown in this figure is the gain in frequency range at which the acoustic signal is measurable due to the cavities. Although SNR is an important metric it is dependent on the signal level (and also the background noise level). It is more important to look at the transfer function for the acoustic and hydrodynamic cases.

This is depicted in Fig. 8, where it is shown that the cavities attenuate the hydrodynamic noise from the TBL more significantly than their effect on the acoustic signal. Also in the low frequency range the TBL fluctuations are found to be attenuated while there is minimal effect on the acoustic signal. The transfer function for the acoustic signal shows a different shape compared to that of the TBL pressure fluctuations. This highlights the fact that the

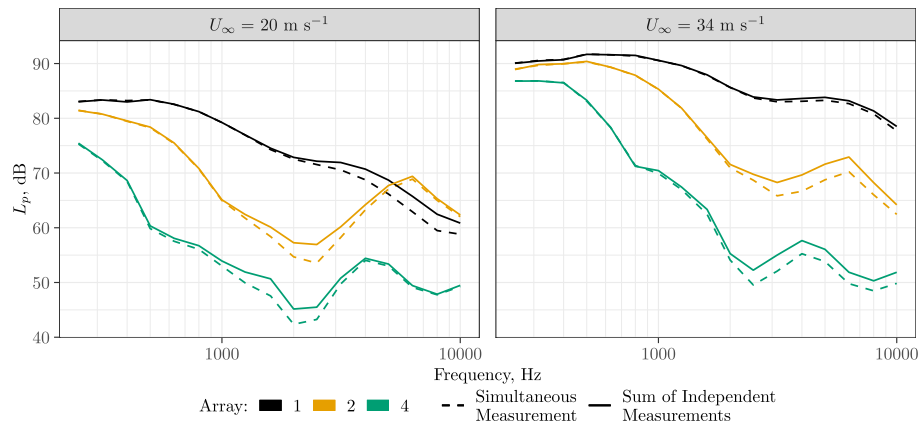


Fig. 6. Comparison between the single microphone measurement for the case where the TBL was present simultaneously with the acoustic source and the summation of the independently measured TBL only and acoustic source only measurements. The summation of independent measurements was calculated by adding the acoustic powers (i.e. before transforming to the decibel scale). Array 3 is not shown to improve readability.

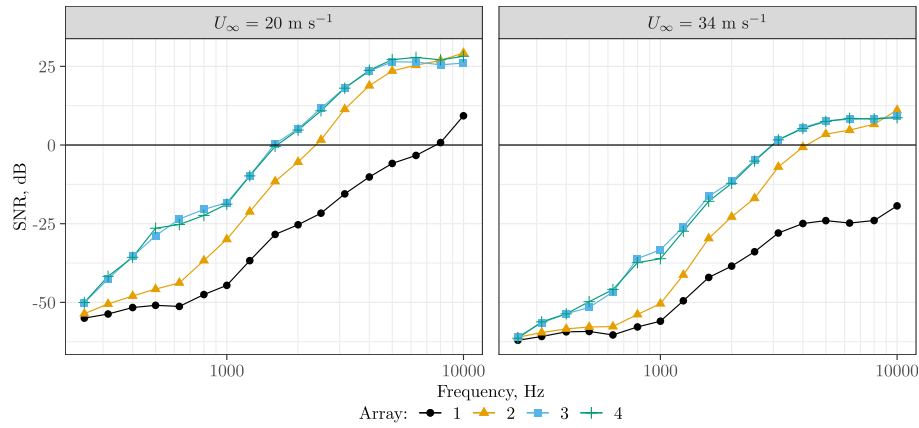


Fig. 7. SNR for a single microphone for each array for the 20 ms⁻¹ and 34 ms⁻¹ cases.

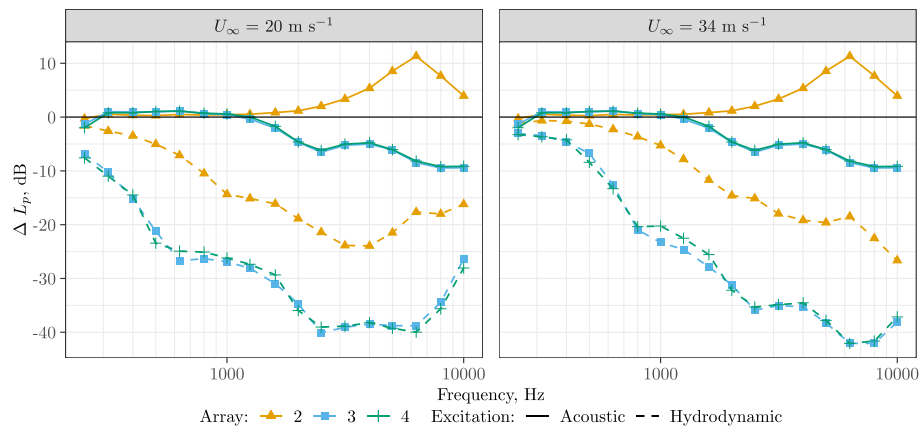


Fig. 8. Acoustic and hydrodynamic transfer functions for the individual cavities for the 20 ms⁻¹ and 34 ms⁻¹ cases.

acoustic and hydrodynamic induced fluctuations measured by the microphone within the cavity have different mechanisms. For frequencies below 3 kHz, the hydrodynamic component of the TBL noise is dominant as evident by its different behavior when compared to the acoustic wave case. However, above 3 kHz, the TBL measurements show a slightly similar behavior as for the acoustic only case suggesting that the acoustic component of the TBL noise may be dominant at the microphone position. This is especially noticeable for the peak at 6 kHz for array 2. A similar conclusion can be drawn from Fig. 4c where a collapsing curve with respect to the Strouhal number indicates hydrodynamic behavior and deviations suggest acoustic phenomena are present.

3.4.2. Microphone array

The increase in SNR due to the cavities, as discussed in the previous section, is further improved by the application of CFDBF to the entire microphone array. Fig. 9 illustrates the source map plot of each array for the case with $U_\infty = 34 \text{ ms}^{-1}$ for the 2 kHz one-third-octave band. In this case the speaker is emitting sound and flow is present over the array. The integrated frequency spectra over a ROI, defined as square $0.2 \text{ m} \times 0.2 \text{ m}$ box centered at the speaker location, are obtained with the SPI method [16,27,28]. The acoustic array data were also processed by using EHR-CLEAN-SC [31,5] and functional projection beamforming [32,33], but no major differences were found in comparison with CFDBF. The beamwidth and dynamic range were shown to be independent of cavity geometry and correspond with predictions made during the array design process [34].

For arrays 1 and 2 (Fig. 9a and b), the source localization fails due to the poor SNR at this frequency band. The L_p values of array 1 are also considerably higher than for the other arrays due to the dominance of TBL noise. Arrays 3 and 4 (Fig. 9c and d) provide similar source maps with the speaker clearly identified at its correct location. Array 3 provides a slightly cleaner source map, with fewer and lower sidelobes.

Fig. 10 depicts the source maps for the case with $U_\infty = 34 \text{ ms}^{-1}$ but now for the 4 kHz one-third-octave band. Once again, array 1 (Fig. 10a) is not able to properly localize the speaker due to the poor SNR. The L_p values are again considerably higher than for the rest of the arrays. This time, arrays 2–4 (Fig. 10b–d) offer very similar source maps with the speaker clearly identified at its correct location and with similar sidelobe patterns.

To quantify the SNR increase due to the application of CFDBF, a similar approach as in the previous section was taken. Now $L_{p,\text{signal}}$ is obtained from the integration of the source map for the source only case and $L_{p,\text{TBL}}$ is obtained from the integration of the source map for the flow only case at the same source location. Fig. 11 highlights the improvement over the single microphone SNR. The application of beamforming improves the SNR by a maximum of 20 dB and the usable frequency range increases significantly. This figure also shows the frequency range in which we can reconstruct the source level from the beamforming plot. For determining these levels, the correction for the acoustic transfer function (Fig. 5b) was applied.

Fig. 12 shows the impact beamforming coupled with different cavity designs has on acoustic measurements for all arrays. This

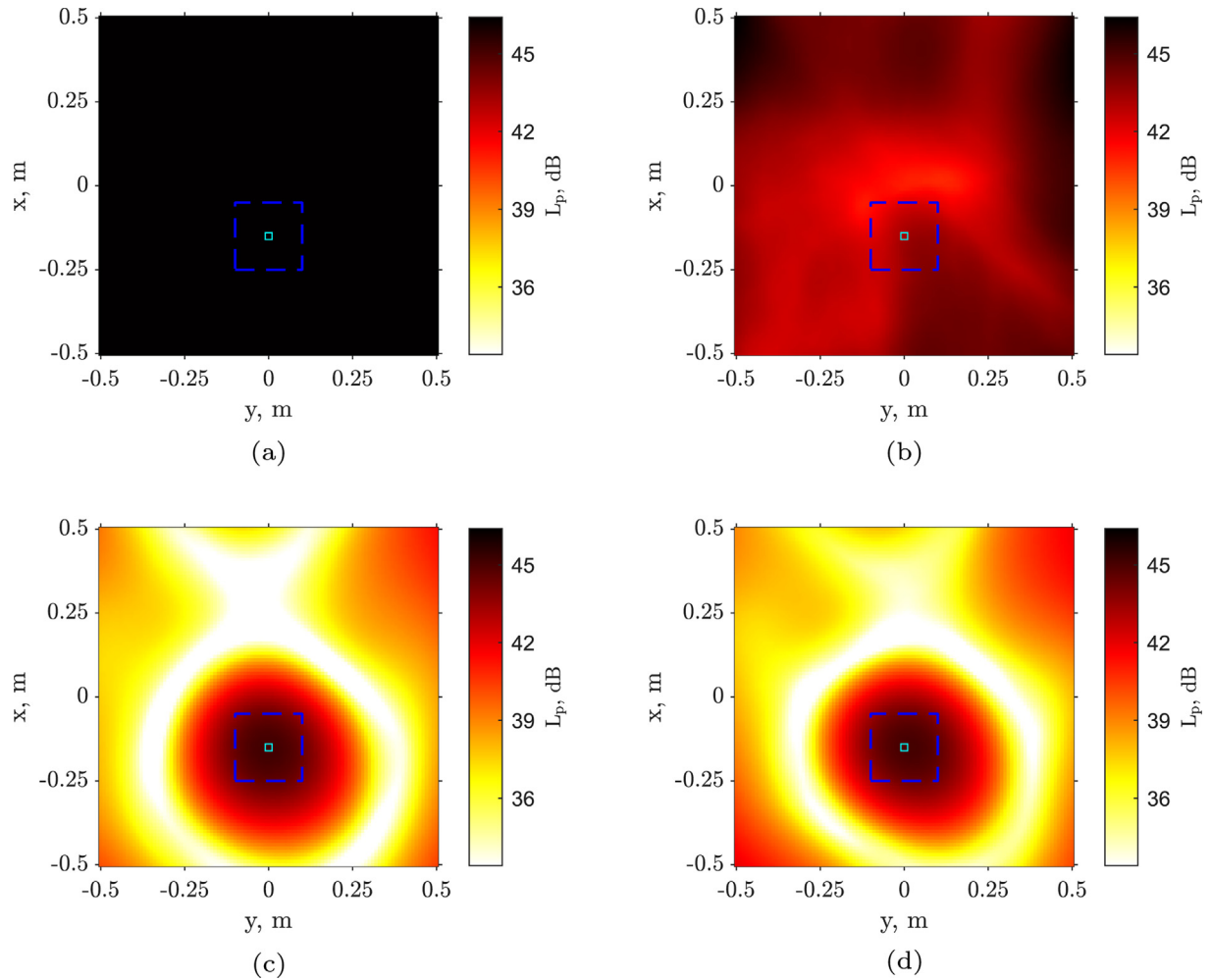


Fig. 9. CFDBF source maps for the case with the speaker for the 2 kHz one-third-octave band and $U_{\infty} = 34 \text{ ms}^{-1}$ for (a) array 1, (b) array 2, (c) array 3, and (d) array 4. The ROI is depicted as a dashed blue square. ΔL_p correction applied.

figure also indicates the minimum frequency threshold for being able to reconstruct the correct source level. The signal of interest is represented by the solid lines which are the one-third-octave band spectra emitted by the speaker with no flow ($U_{\infty} = 0 \text{ ms}^{-1}$). The frequency threshold is defined as the one-third-octave band where the difference between the case with flow and the case without flow is less than 3 dB. These are denoted with a vertical short and long dashed lines, for the cases with $U_{\infty} = 20 \text{ ms}^{-1}$ and 34 ms^{-1} , respectively. However, near these frequency thresholds, localizing the sound source with beamforming is still challenging due to the fact that the acoustic signal is within 3 dB of the TBL noise. For array 1 (Fig. 12a), the sound levels emitted by the speaker are lower than those of the TBL noise for the 34 ms^{-1} case which means the baseline case cannot detect the signal of interest. Array 2 is a clear improvement, detecting the signal after 1.25 kHz for 20 ms^{-1} , and after 2 kHz for the 34 ms^{-1} case. Arrays 3 and 4, with the melamine walls, reconstruct the signal after 1 kHz and 1.6 kHz for the 20 and 34 ms^{-1} cases, respectively. For the low frequencies it is not possible to retrieve the signal of interest for this case due to the low signal levels with respect to the TBL noise levels.

The three cavity geometries enable the source to be measured at a lower frequency threshold, which directly corresponds to a decrease in the measured TBL noise level. Since arrays 3 and 4 reduced the measured TBL noise levels the most, by 40 dB, they

are able to identify the source at a lower frequency than array 2. This is despite the fact they slightly attenuate the acoustic signal (Fig. 5). The microphone arrays and acoustic imaging techniques allow for the extraction of accurate sound pressure levels even in conditions where a single microphone would have negative SNR values [35,7]. This ability is, nonetheless, limited to certain SNR values depending on the array geometry and experimental conditions, as well as the number of microphones and data acquisition time [36]. In order to evaluate a more practical case, a distributed acoustic source with higher levels at these low frequencies was investigated in the next section.

3.5. Distributed acoustic source measurements

The source maps for the flat plate immersed in a flow with a velocity of 34 ms^{-1} and the 4 kHz one-third-octave band are shown in Fig. 13. The flat plate is denoted with cyan lines and the ROI is depicted as a dashed blue rectangle. Similar to the test with the speaker, array 1 is not able to correctly localize the distributed noise source generated by the flat plate's trailing edge due to the insufficient SNR. Array 2 shows a distributed sound source along the trailing edge, together with the horizontal reflections due to the support side plates as well as their self noise. Arrays 3 and 4 perform similarly but their distributed source at the trailing edge

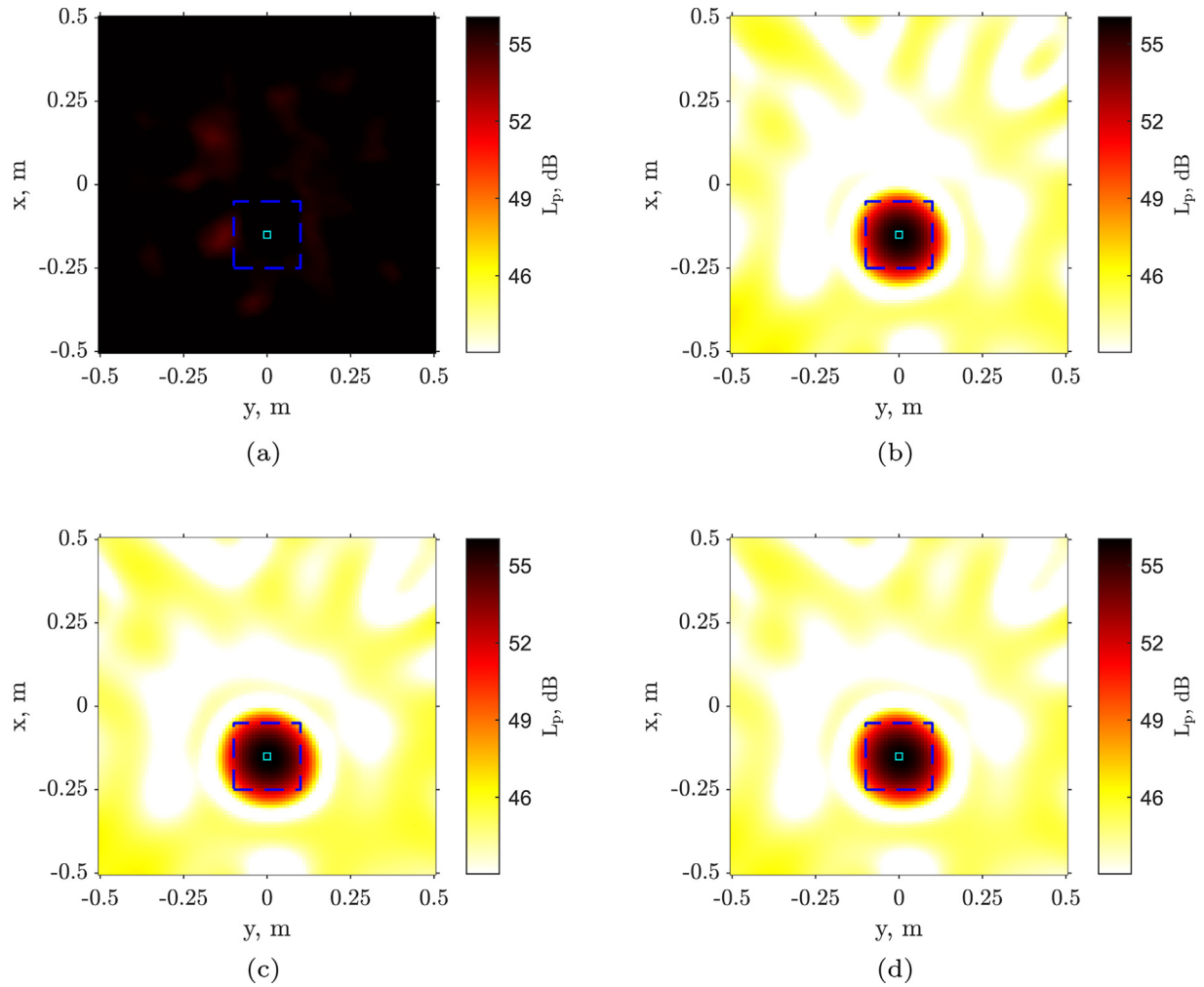


Fig. 10. CFDFB source maps for the case with the speaker for the 4 kHz one-third-octave band and $U_\infty = 34 \text{ ms}^{-1}$ for (a) array 1, (b) array 2, (c) array 3, and (d) array 4. The ROI is depicted as a dashed blue square. ΔL_p correction applied.

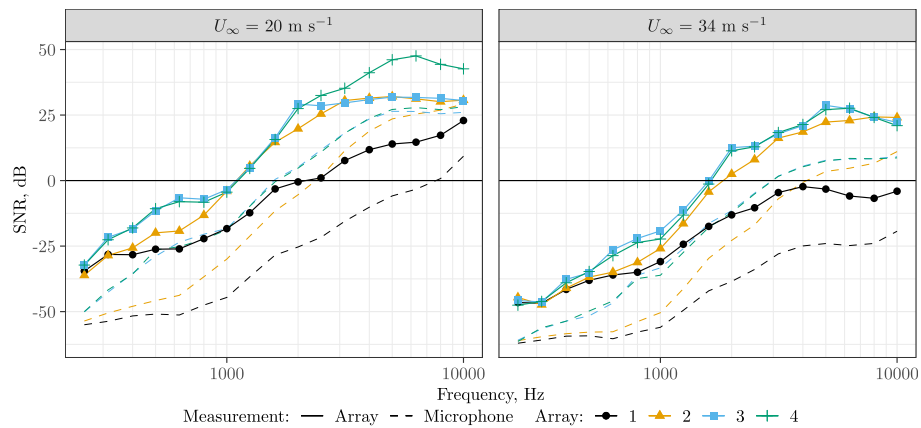


Fig. 11. SNR for each array when using CFDFB and for the single microphone baseline for the 20 ms^{-1} and 34 ms^{-1} cases.

is relatively stronger compared to the sidelobes present in the rest of the map.

The one-third-octave band spectra integrated within the ROI covering the trailing edge of the flat plate (see dashed blue rectangle in Fig. 13) are depicted in Fig. 14 for the four arrays and the two flow velocities. The L_p values shown are referred to the baseline of

array 1 using the ΔL_p correction shown in Fig. 5b. In addition, the spectra were corrected in order to consider a normalized span of 1m given that the ROI is 0.3 m wide compared to the 0.4 m wide plate. Additionally, the spectra were reduced by 6 dB to account for the differences between the array and the free-field measurements, see Fig. 5b. It can be observed that the spectra of arrays 2

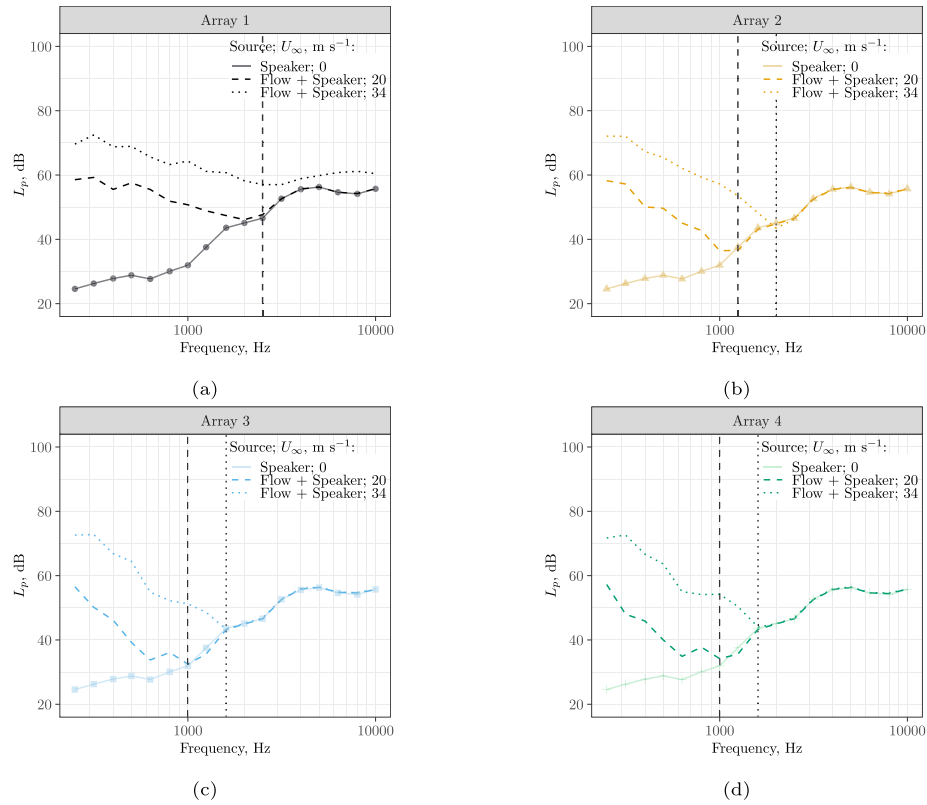


Fig. 12. Comparison of the one-third-octave band spectra emitted by the speaker with the TBL noise spectra for $U_\infty = 20 \text{ ms}^{-1}$ and $U_\infty = 34 \text{ ms}^{-1}$ with and without the speaker as measured by beamforming at the same source location: (a) array 1, (b) array 2, (c) array 3, and (d) array 4. Acoustic calibration from Fig. 5b is applied to all cases. Vertical lines are the frequency for each velocity at which the signal is detected.

to 4 are in good agreement for the case with $U_\infty = 20 \text{ ms}^{-1}$ (Fig. 14a) throughout the whole frequency range. For the case with $U_\infty = 34 \text{ ms}^{-1}$ (Fig. 14b), the spectrum measured by array 2 presents L_p values up to 7 dB higher than those by arrays 3 and 4, especially at lower frequencies. This is most likely due to the lower TBL noise attenuation by array 2, compared to arrays 3 and 4 (see Fig. 12). Array 1, on the other hand, shows consistently higher values (up to 15 dB higher for some frequency bands) than the other arrays. This is due to the poor SNR of this array, which does not allow for the correct identification of the trailing-edge noise.

The distributed source acoustic measurements are compared against the Brooks, Pope and Marcolini (BPM) semi-empirical model [37]. The model predicts the turbulent boundary layer trailing edge noise and vortex shedding noise contributions among others. The total L_p predicted for the flat plate is in good agreement with that measured by arrays 2–4, as seen in Fig. 14. These arrays detected a spectral peak at 2 kHz for the 20 ms^{-1} case and at 4 kHz for the 34 ms^{-1} case. These peaks agree with the BPM predictions for the vortex shedding contribution. The baseline array, array 1, was unable to identify any vortex shedding. However, these measurements are limited by the high noise levels from the TBL.

3.6. Effect of cavity geometry on signal coherence

CFDBF is based on the phase delays of the arrival of an acoustic wave at different microphones. Therefore losses of coherence within the travel time of the sound waves are detrimental for the beamforming results. This is why the effect of cavity geometry on the coherence is important to quantify. The coherence of each microphone signal with respect to that of the center microphone, and with respect to all other microphone signals was calculated

using Eq. 1 where P_{xy} is the cross-spectral density of a pair of signals x and y and P_{xx} and P_{yy} are the power spectral densities.

$$C_{xy} = \frac{|P_{xy}|^2}{P_{xx}P_{yy}} \quad (1)$$

The aim is to determine how the relative cavity locations, flow conditions, and cavity geometry influence the coherence of the acoustic signals and whether this affects the performance of acoustic imaging. Additionally, in order to determine whether further improvements in beamforming can be achieved, coherence weighting was investigated using the approach discussed in Amaral et al. [18]. The reasoning for applying this method is that due to the expected higher coherence of the optimal cavities, more microphones are part of the beamforming process. The microphone signals are multiplied by a weighting factor between 0 and 1 based on their relative coherence with the other microphones. This approach (results not shown here) did not lower the frequency threshold at which the signal could be detected. This is due to the fact that at SNR values near zero, the incoherent noise sources are at a similar level as the coherent sources. The resulting coherence weighting of the microphones reduces the weighting for all microphones and, thus, reduces the measured signal and noise levels equally.

Fig. 15 depicts the coherence of all cavities compared against all others sorted with respect to their relative distances in the streamwise, Δx , and spanwise, Δy , directions. These results are with flow, $U_\infty = 34 \text{ ms}^{-1}$ and with the speaker for array 4 for the 4 kHz band. This figure is representative of all arrays when the acoustic signal is dominant. When the TBL is dominant, the coherence for all cavities is low, as expected. This representative figure shows that coherence across the array is consistent and that cavity geometry has

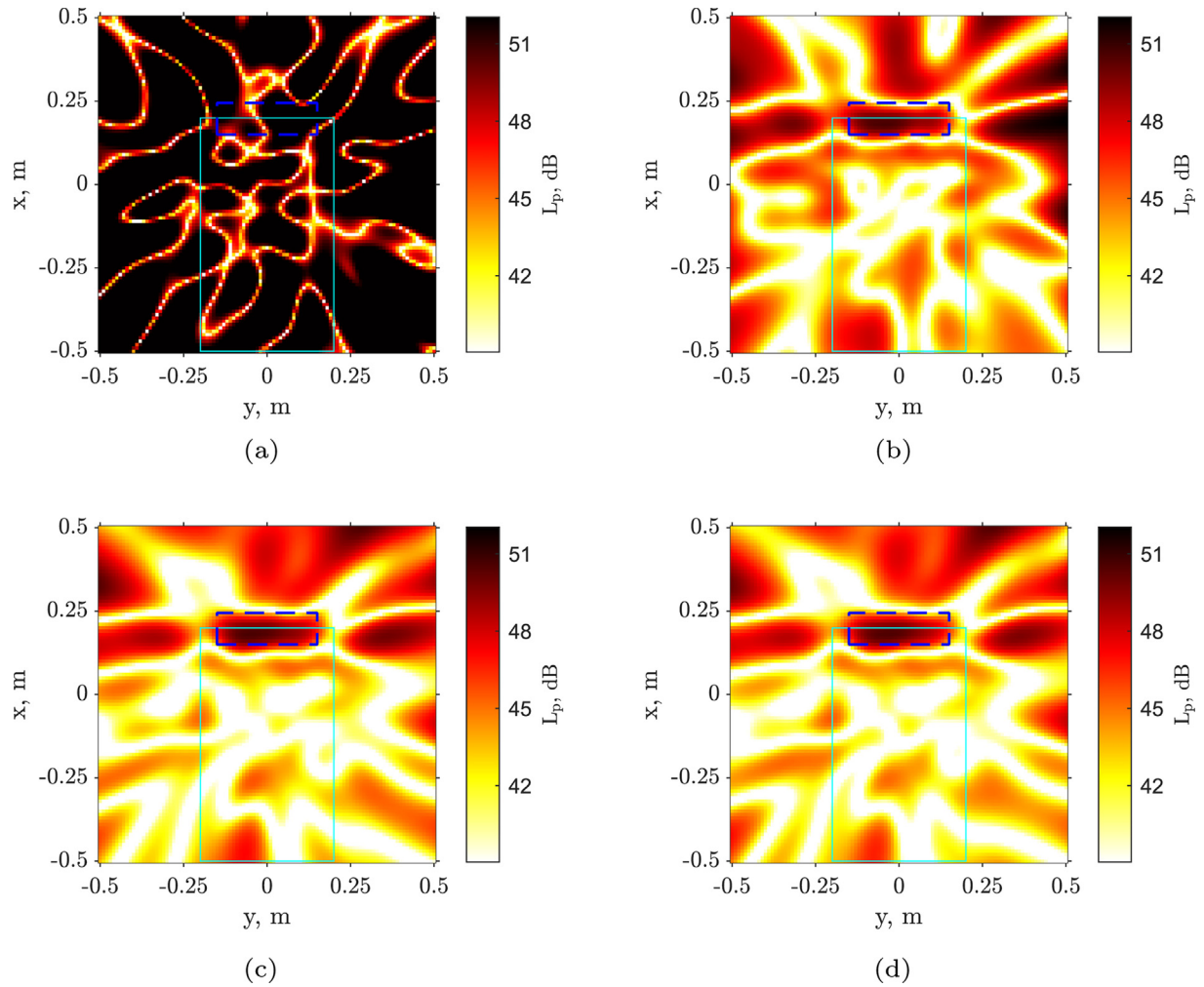


Fig. 13. CFDBF source maps for the test with the flat plate for the 4 kHz one-third-octave band and $U_\infty = 34 \text{ ms}^{-1}$ for (a) array 1, (b) array 2, (c) array 3, and (d) array 4. The flat plate is denoted with cyan lines and the ROI is depicted as a dashed blue rectangle. ΔL_p correction applied.

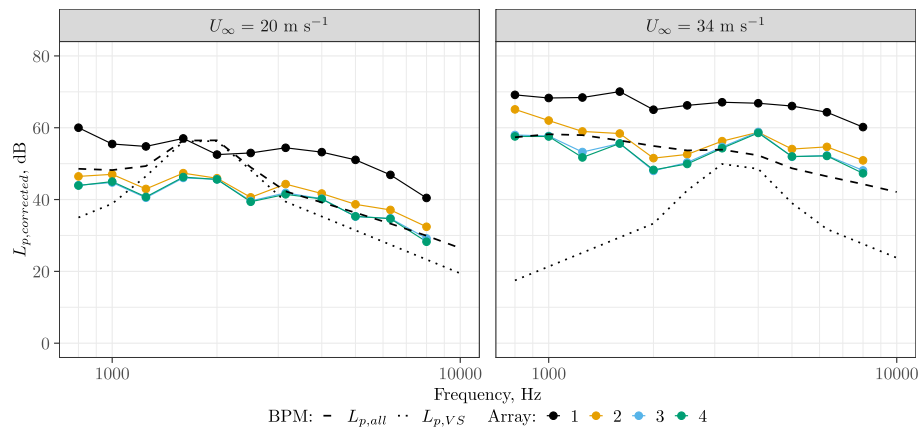


Fig. 14. One-third-octave band spectra emitted by the trailing edge of the flat plate integrated within the ROI for the four arrays and for $U_\infty = 20 \text{ ms}^{-1}$ and $U_\infty = 34 \text{ ms}^{-1}$ compared with the BPM model. $L_{p,all}$ is the total BPM prediction and $L_{p,vs}$ is the predicted vortex shedding contribution. The L_p values are referred to the baseline of array 1 using the ΔL_p correction shown in Fig. 5b.

no detectable influence on the coherence. This behavior is similar for all other arrays. Looking more closely at two representative cases, Fig. 16 shows the coherence for array 1, Fig. 16a, and array 4, Fig. 16b, with respect to frequency for three different microphone pairs for the case with the speaker and $U_\infty = 34 \text{ ms}^{-1}$.

Fig. 16c and d are the cases for arrays 1 and 4 respectively with the speaker only and no flow. The selected pairs are the two closest cavities ($\Delta x = -0.05 \text{ m}$, $\Delta y = 0.06 \text{ m}$), the largest streamwise distance ($\Delta x = -0.36 \text{ m}$, $\Delta y = 0.08 \text{ m}$), and the largest spanwise distance ($\Delta x = 0.05 \text{ m}$, $\Delta y = -0.33 \text{ m}$). At 100 Hz, flow noise is

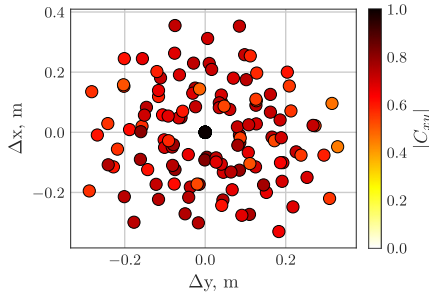


Fig. 15. Comparison of the coherence between all cavity locations with respect to all others, sorted by relative distance in the stream-wise and span-wise directions. Coherence is calculated for the case with the speaker and flow, $U_\infty = 34 \text{ ms}^{-1}$ for array 4 at 4 kHz.

dominant and coherence is dependent on the boundary layer coherence lengths for both arrays. For array 4, the coherence values increase only once the TBL noise is 6 dB beneath the acoustic source's signal which occurs for frequencies higher than 2 kHz. Array 1 does not meet this threshold resulting in low coherence, irrespective of frequency. For comparison, the cases with only the speaker, Fig. 16c and d, show coherence values close to 1 for frequencies above 1 kHz. The conclusions drawn from this analysis are as follows:

- The resulting normalized coherence between microphones approaches 1 and is relatively consistent with respect to distance in the streamwise direction for arrays 2, 3, and 4.
- Due to potential three-dimensional flow effects present at the edges of the plate, the cavities near the edge, $|\Delta y| > 0.3 \text{ m}$ have a reduced coherence value of 0.5.

- The coherence calculations for the cases with the acoustic source and without flow show that irrespective of distance, all cavities have a coherence of almost 1.
- Arrays 3 and 4 have higher coherence compared to array 2, which was higher than array 1, for the case with a speaker and flow.
- The trends with respect to relative distance are independent of the type of cavity employed.

3.6.1. Effect of stainless steel cloth covering

The stainless steel cloth that covers the cavities in arrays 2, 3, and 4 improves the SNR by reducing the influence of the TBL hydrodynamic fluctuations as shown previously in Fig. 4. Given the low acoustic impedance of the cloth, 0.15, normalized with respect to air, a negligible change in the acoustic signal's amplitude is expected due to the cloth. Fig. 16d shows the relative effect of the cavity geometry and cloth on the acoustic signal. Compared with the baseline case, Fig. 16c, where there is no cloth present, there is no significant change in coherence of the acoustic signal due to the cloth. Both arrays show coherence values close to 1 above 1 kHz and a reduction for lower frequencies where the acoustic signal amplitude is lower and outside of the speaker's intended frequency range. From these results it is concluded that the cloth has a negligible impact on the signal coherence and thus the acoustic beamforming results.

4. Conclusions

This work quantifies the impact of cavity geometry on the SNR, and on the accuracy of acoustic imaging results for microphone arrays. Three cavities, one with a hard walled countersink and

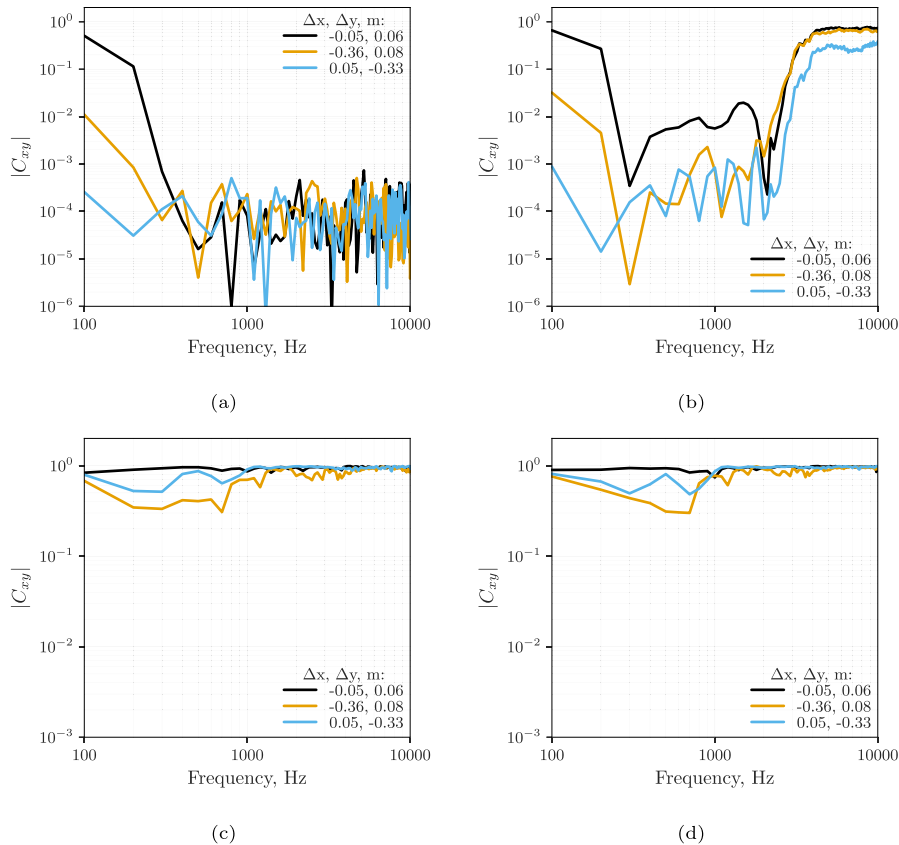


Fig. 16. Coherence plotted with respect to narrow band ($\Delta f = 25 \text{ Hz}$) frequencies for cavity pairs at three different separation distances. Coherence is calculated for the following cases: (a) array 1, with the speaker and flow, $U_\infty = 34 \text{ ms}^{-1}$; (b) array 4, with the speaker and flow, $U_\infty = 34 \text{ ms}^{-1}$; (c) array 1, speaker only; and (d) array 4, speaker only.

two conical cavities with melamine walls, all covered with a high thread count stainless steel cloth, are compared with a baseline flush-mounted microphone array. Each array featured 16 microphones in the same layout. These arrays were mounted flush with an open jet wind-tunnel nozzle and used to measure white noise emitted by a speaker mounted outside of the flow and a distributed source from the trailing edge of a flat plate placed within the flow. Conventional frequency domain beamforming with diagonal removal was used to determine the effect cavity geometry has on the acoustic signal, TBL, and resulting SNR.

These cavities reduced the amount of measured TBL noise while minimizing the effect on the acoustic signal, thus increasing the SNR. The cavities with melamine foam (arrays 3 and 4) reduced the TBL noise by up to 40 dB compared to the flush-mounted array. The hard walled cavity, array 2, reduced the TBL noise by up to 25 dB. However, the hard walled cavity amplified the signal by 10 dB at certain frequencies due to an acoustic mode, whereas the soft walled cavities caused a reduction between 5 and 10 dB at certain frequencies compared to the flush array. Overall, the SNR was increased due to the TBL being attenuated more than the acoustic signal.

When comparing the hydrodynamic and acoustic transfer functions, the TBL's hydrodynamic phenomena appears to be dominant below 3 kHz. Above 3 kHz, its acoustic component begins to show similar behavior as the acoustic transfer function, seen for the speaker only case. However, the interplay between the TBL's hydrodynamic and acoustic components is complex and requires further study.

The resulting impact on SNR is that the CFDBF has an additional 20 dB improvement over the single microphone for the same cavity geometry. This improvement is seen in the beamforming source maps and integrated L_p where the recessed arrays detected the acoustic signal when the flush-mounted array could not. Moreover, arrays 3 and 4 detected the signal at a frequency threshold 400 Hz lower than array 2.

The coherence of the acoustic signal for all cavity geometries was consistent with respect to the cavity position in the array. The stainless steel covering has minimal impact on the acoustic coherence and, thus, on the beamforming performance. Coherence improves with frequency for arrays 2 to 4 due to the reduction of incoherent TBL noise.

The improvements using the cavities, especially in arrays 3 and 4, are also seen in the flat plate measurements. The source maps using these arrays successfully imaged the trailing edge noise whereas the baseline array did not. Additionally, these arrays identified a spectral peak from vortex shedding that agreed with the BPM model. The baseline case, array 1, was unable to distinguish these peaks from the TBL noise.

These results show that using an appropriately designed microphone cavity augments the acoustic imaging capabilities of a microphone array using CFDBF signal processing. Beamforming with diagonal removal reduces the incoherent TBL noise by up to 20 dB. Adding cavities further improves these measurements by reducing the TBL noise by an additional 40 dB for the melamine cavities. By using optimized cavity geometries with larger diameter microphone arrays with more microphones, even greater improvements to SNR are expected. This approach potentially enables testing of acoustic sources whose sound levels are near the background turbulent boundary layer noise levels. However, more work is needed on understanding the relationship between the hydrodynamic TBL behavior and the cavity geometry to better optimize these cavities.

CRedit authorship contribution statement

Colin VanDercreek: Conceptualization, Methodology, Software, Investigation, Data curation, Writing - original draft, Writing -

review & editing, Formal analysis, Visualization, Project administration. **Roberto Merino-Martínez:** Methodology, Writing - original draft, Software, Formal analysis, Visualization, Investigation. **Pieter Sijtsma:** Writing - review & editing, Validation, Formal analysis. **Mirjam Snellen:** Writing - review & editing, Funding acquisition, Project administration, Supervision.

Declaration of Competing Interest

The authors declare that they have no known competing financial interests or personal relationships that could have appeared to influence the work reported in this paper.

Acknowledgements

This work is part of the research programme THAMES with project number 15215, which is (partly) financed by the Dutch Research Council (NWO). The authors would also like to acknowledge the THAMES project partners for their insight and assistance.

References

- [1] Stoker R, Guo Y, Streett C, Burnside N. Airframe noise source locations of a 777 aircraft in flight and comparisons with past model-scale tests. In: 9th AIAA/CEAS aeroacoustics conference, May 12–14 2003, Hilton Head, South California, USA, 2003, AIAA paper 2003–3232. doi:10.2514/6.2003-3232.
- [2] Merino-Martínez R, Sijtsma P, Snellen M, Ahlefeldt T, Antoni J, Bahr CJ, Blacodon D, Ernst D, Finez A, Funke S, Geyer TF, Haxter S, Herold G, Huang X, Humphreys WM, Leclère Q, Malgoezar A, Michel U, Padois T, Pereira A, Picard C, Sarraji E, Siller H, Simons DG, Spehr C. A review of acoustic imaging methods using phased microphone arrays (part of the Aircraft Noise Generation and Assessment special issue). CEAS Aeronaut J 2019;10(1):197–230. <https://doi.org/10.1007/s13272-019-00383-4>.
- [3] Mueller T. Aeroacoustic measurements. Berlin, Germany: Springer Science & Business Media; 2002, ISBN 978-3-642-07514-8.
- [4] Merino-Martínez R, Neri E, Snellen M, Kennedy J, Simons DG, Bennett GJ. Comparing flyover noise measurements to full-scale nose landing gear wind-tunnel experiments for regional aircraft. In: 23rd AIAA/CEAS aeroacoustics conference, June 5–9 2017, Denver, Colorado, USA, 2017, AIAA paper 2017–3006. doi:10.2514/6.2017-3006.
- [5] Sijtsma P, Merino-Martínez R, Malgoezar AMN, Snellen M. High-resolution CLEAN-SC: theory and experimental validation. Int J Aeroacoust 16 (4–5): 2017; 274–298. SAGE Publications Ltd., London, United Kingdom. doi:10.1177/1475472X17713034.
- [6] Merino-Martínez R, Neri E, Snellen M, Kennedy J, Simons DG, Bennett GJ. Analysis of nose landing gear noise comparing numerical computations, prediction models and flyover and wind-tunnel measurements. In: 24th AIAA/CEAS aeroacoustics conference, June 25–29 2018, Atlanta, Georgia, USA, 2018, AIAA paper 2018–3299. doi:10.2514/6.2018-3299.
- [7] Merino-Martínez R, Luesutthiviboon S, Zamponi R, Rubio Carpio A, Ragni D, Sijtsma P, Snellen M, Schram C. Assessment of the accuracy of microphone array methods for aeroacoustic measurements. J Sound Vib 2020;470(115176):1–24. <https://doi.org/10.1016/j.jsv.2020.115176>.
- [8] Jaeger SM, Horne W, Allen C. Effect of surface treatment on array microphone self-noise. In: 6th AIAA/CEAS aeroacoustics conference, June 12–14 2016, Lahaina, HI, USA, 2000, AIAA paper 2000–1937. doi:10.2514/6.2000-1937.
- [9] Fleury V, Coste L, Davy R, Mignosi A, Cariou C, Prosper J-M. Optimization of microphone array wall mountings in closed-section wind tunnels. AIAA J 2012;50(11):2325–35. <https://doi.org/10.2514/1.j051336>.
- [10] VanDercreek CP, Amiri-Simkooei A, Snellen M, Ragni D. Experimental design and stochastic modeling of hydrodynamic wave propagation within cavities for wind tunnel acoustic measurements. Int J Aeroacoust 2019;18(8):752–79. <https://doi.org/10.1177/1475472X19889949>.
- [11] Remillieux MC, Crede ED, Camargo HE, Burdisso RA, J DW, Rasnick M, van Seeters P, Chou A. Calibration and demonstration of the New Virginia Tech Anechoic wind tunnel. In: 14th AIAA/CEAS aeroacoustics conference (29th AIAA Aeroacoustics Conference), May 5–7, 2008, Vancouver, British Columbia, Canada, 2008, AIAA paper 2008–2911. doi:10.2514/6.2008-2911.
- [12] Horne WC, Burnside NJ. Development of new wall-mounted and strut-mounted phased microphone arrays for acoustic measurements in closed test-section wind tunnels. In: 21st AIAA/CEAS aeroacoustics conference 2015. <https://doi.org/10.2514/6.2015-2975>.
- [13] Shin H-C, Graham WR, Sijtsma P, Andreou C, Faszler AC. Implementation of a phased microphone array in a closed-section wind tunnel. AIAA J 2007;45(12):2897–909. <https://doi.org/10.2514/1.30378>.
- [14] Rienstra SW. Fundamentals of duct acoustics. Technische Universiteit Eindhoven 2015.
- [15] van Veen BD, Buckley KM. Beamforming: a versatile approach to spatial filtering. IEEE ASSP Mag 1988;5(2):4–24. <https://doi.org/10.2514/1.C033020>.

- [16] Sijtsma P. Phased array beamforming applied to wind tunnel and fly-over tests, Tech. Rep. NLR-TP-2010-549, National Aerospace Laboratory (NLR), Anthony Fokkerweg 2, 1059 CM Amsterdam, P.O. Box 90502, 1006 BM Amsterdam, The Netherlands (December 2010)..
- [17] Sijtsma P, Dinselmeyer A, Antoni J, Leclerc Q. Beamforming and other methods for denoising microphone array data. In: 25th AIAA/CEAS aeroacoustics conference. Delft, Netherlands: American Institute of Aeronautics and Astronautics; 2019. <https://doi.org/10.2514/6.2019-2653>.
- [18] Amaral FR, Pagani CC, Medeiros MAF. Improvements in closed-section wind-tunnel beamforming experiments of acoustic sources distributed along a line. *Appl Acoust* 2019;156:336–50. <https://doi.org/10.1016/j.apacoust.2019.07.022>.
- [19] Merino-Martínez R, Rubio Carpio A, Lima Pereira LT, van Herk S, Avallone F, Kotsonis M, Ragni D. Aeroacoustic design and characterization of the 3D-printed, open-jet, anechoic wind tunnel of Delft University of Technology. *Appl Acoust* 2020;170(107504):1–16. <https://doi.org/10.1016/j.apacoust.2020.107504>.
- [20] Merino-Martínez R. Microphone arrays for imaging of aerospace noise sources, Ph.D. thesis, Delft University of Technology, ISBN: 978-94-028-1301-2 (2018). doi:10.4233/uuid:a3231ea9-1380-44f4-9a93-dbbd9a26f1d6..
- [21] Sarraji E. A Generic approach to synthesize optimal array microphone arrangements. In: BeBeC; 2016..
- [22] Luesutthiviboon S, Malgouezar A, Snellen M, Sijtsma P, Simons DG. Improving source discrimination performance by using an optimized acoustic array and adaptive high-resolution CLEAN-SC beamforming. In: 7th Berlin beamforming conference, March 5–6 2018, Berlin, Germany, GFal, e.V., Berlin, 2018, BeBeC-2018-D07..
- [23] G.R.A.S. Sound & Vibration – 40PH CCP Free-field array microphone, <http://www.gras.dk/products/special-microphone/array-microphones/product/178-40ph>, accessed in March 2017..
- [24] G.R.A.S. Sound & Vibration – 42AA Pistonphone class 1, <https://www.gras.dk/products/calibration-equipment/reference-calibrator/product/255-42aa>, accessed in March 2017..
- [25] Morse PM, Ingard KU. Theoretical acoustics, McGraw-Hill, New York SE – xix, 927 pages illustrations 23 cm; 1968..
- [26] Visaton – Speaker K 50 SQ – 8 Ohm, <http://www.visaton.de/en/products/fullrange-systems/k-50-sq-8-ohm>, accessed in March 2017..
- [27] Merino-Martínez R, Sijtsma P, Snellen M. Inverse integration method for distributed sound sources. In: 7th Berlin beamforming conference, March 5–6 2018, Berlin, Germany, GFal, e.V., Berlin, 2018, BeBeC-2018-S07..
- [28] Merino-Martínez R, Sijtsma P, Rubio Carpio A, Zamponi R, Luesutthiviboon S, Malgouezar AMN, Snellen M, Schram C, Simons DG. Integration methods for distributed sound sources. *Int J Aeroacoust* 2019;18(4–5):444–69. <https://doi.org/10.1177/1475472X19852945>.
- [29] Cengel YA, Cimbala JM. *Fluid mechanics: fundamentals and applications*. 3rd ed. New York: McGraw Hill; 2014.
- [30] Rubio Carpio A, Avallone F, Ragni D, Snellen M, van der Zwaag S. 3D-printed perforated trailing edges for broadband noise abatement. In: 25th AIAA/CEAS aeroacoustics conference, May 20–24 2019, Delft, The Netherlands, 2019, AIAA paper 2019-2458. doi:10.2514/6.2019-2458..
- [31] Luesutthiviboon S, Malgouezar AMN, Merino-Martínez R, Snellen M, Sijtsma P, Simons DG. Enhanced HR-CLEAN-SC for resolving multiple closely spaced sound sources. *Int J Aeroacoust* 2019;18(4–5):392–413. <https://doi.org/10.1177/1475472X19852938>.
- [32] Dougherty RP. Determining spectra of aeroacoustic sources from microphone array data. In: 25th AIAA/CEAS aeroacoustics conference, May 20–23 2019, Delft, The Netherlands, 2019, AIAA paper 2019-2745. doi:10.2514/6.2019-2745..
- [33] Merino-Martínez R, Herold G, Snellen M, Dougherty RP. Assessment and comparison of the performance of functional projection beamforming for aeroacoustic measurements. In: 8th Berlin beamforming conference, March 2–3 2020, Berlin, Germany, GFal, e.V., Berlin, 2020, BeBeC-2020-S7..
- [34] VanDercreek CP, Merino-Martínez R, Snellen M, Simons DG. Comparison of cavity geometries for a microphone array in a open-jet wind-tunnel experiment. In: 8th Berlin beamforming conference, March 2–3 2020, Berlin, Germany, GFal, e.V., Berlin, 2020, BeBeC-2020-D7..
- [35] Sarraji E, Herold G, Sijtsma P, Merino-Martínez R, Malgouezar AMN, Snellen M, Geyer TF, Bahr CJ, Porteous R, Moreau DJ, Doolan CJ. A microphone array method benchmarking exercise using synthesized input data. In: 23th AIAA/CEAS aeroacoustics conference, June 5–9 2017, Denver, CO, USA, 2017, AIAA paper 2017-3719. doi:10.2514/6.2017-3719..
- [36] Sijtsma P. Accuracy criterion for source power integration with CSM diagonal removal. In: BeBeC, Berlin; 2020. p. 1–15.
- [37] Brooks TF, Pope DS, Marcolini MA. Airfoil self-noise and prediction, Tech. Rep. NASA Reference Publication 1218, NASA Reference Publication 1218; 1989.